International Journal of Heat and Fluid Flow 30 (2009) 421–434

Contents lists available at ScienceDirect

International Journal of Heat and Fluid Flow

journal homepage: www.elsevier.com/locate/ijhff

Large-Eddy simulations of circular synthetic jets in quiescent surroundings and in turbulent cross-flow

Don K.L. Wu *, Michael A. Leschziner

Imperial College London, Department of Aeronautics, Prince Consort Road, London SW7 2BY, United Kingdom

ARTICLE INFO

Article history:
Received 12 October 2008
Received in revised form 10 January 2009
Accepted 17 January 2009
Available online 23 February 2009

Keywords:
Synthetic jet
Flow control
Separation control
Turbulent boundary layer
Large-Eddy simulation

ABSTRACT

Large-Eddy simulation (LES) is used to investigate the physical processes involved in the injection of a synthetic (zero-net-mass-flux) jet in quiescent surroundings and into a zero-pressure-gradient, turbulent boundary layer over a flat plate at conditions corresponding to experimental data obtained by others. The former case is studied because it constitutes a key ingredient of the latter. Specifically, it allows the computational framework to be verified, basic properties of synthetic jets to be studied, and the sensitivity of the jet structure to the details of the computational representation of the jet orifice to be investigated. In particular, the validity of representing the circular orifice, within a multi-block H-topology mesh, alternatively, by an equivalent square orifice, or by means of a solid-cell-blocking technique or via local mesh distortion, is examined. The boundary layer ahead of the jet is generated by a separate precursor simulation at a momentum-thickness Reynolds number $Re_\theta = 2380$, providing the main simulation with a full and accurate description of the unsteady conditions at the computational inflow boundary. Time- and phase-averaged results are presented and compared against experimental data.

1. Introduction

Synthetic jets have a demonstrable ability to delay or prevent the onset of separation in an adverse-pressure-gradient boundary layer. Although the net mass injected is zero, vorticity and momentum are introduced, and mixing in the boundary layer is increased, so that the energy/momentum transport towards the wall is enhanced.

In the past, synthetic jets have been studied extensively by experimental means (e.g. Smith and Glezer, 1998; Cater and Soria, 2002; Lee et al., 2003), but computational studies are rarer (e.g. Rizzetta et al., 1999; Vatsa and Turkel, 2006). In the case of jets injected into boundary layers, attention has focused mainly on spanwise-homogeneous configurations (Greenblatt et al. (2006), Krishnan et al. (2006), You et al. (2006), and others). Homogeneity makes this an attractive actuation mode in a laboratory setting and, even more so, for computational validation studies, especially of the RANS variety. However, it is the actuation by means of 3D circular (or similarly shaped) synthetic jets that produces a more effective separation control, per orifice area, by generating strong streamwise vorticity that enhances the mixing within the boundary layer. It is also a more practical option. While a few numerical investigations of fully 3D synthetic jets in turbulent cross-flow have been conducted (e.g. Mallinson et al., 2003), many, if not most, are of the URANS variety. It is arguable, however, that only scale-resolving simulations are capable of capturing the interplay between the unsteady vorticity injected and the turbulent structure in the boundary-layer region to be controlled.

An approach that goes partway towards resolving the turbulent scales of the interaction, namely through the use of Detached-Eddy simulations (DES), was employed by Xia and Qin (2005) to simulate a circular synthetic jet injected into a attached turbulent boundary layer, by reference to experimental data compiled by Schaeffler and Jenkins (2006). Their simulation was able to capture the gross dynamics of the interaction, despite the lack of spectral resolution in the approaching boundary layer. At the orifice, time-averaged results of the exit-velocity profiles and time-history of the velocity at the orifice centre agreed reasonably well with experimental data. Turbulent structures were resolved downstream of the orifice and further away from the wall in the LES regime. The coherent vortical structures, produced by the injection puff, were seen to break down rapidly under the influence of the cross-flow. However, no quantitative analysis of the turbulence physics was provided by the authors. Similarly good agreement with the experimental data for the mean-flow characteristics was achieved in another numerical study conducted by Dandois et al. (2006), who reported several URANS and LES solutions of the same flow of Schaeffler and Jenkins (2006) with varying mesh sizes, time-steps, inlet-boundary conditions and different methods of modelling the dynamics of the actuation. One of the main findings was that even a URANS simulation, on a coarse mesh providing a

* Corresponding author.
E-mail address: d.wu04@imperial.ac.uk (D.K.L. Wu).

0142-727X/$ - see front matter © 2009 Elsevier Inc. All rights reserved.
doi:10.1016/j.ijheatfluidflow.2009.01.007

wall-normal resolution no better than $\Delta y^+ = 309$ in the wake of the jet, was capable of capturing the gross effects of the injection and returning good predictions of the mean-velocity profiles. In contrast, the time-averaged turbulent stresses resulting from the interaction were only accurately resolved when LES was used and when the oncoming turbulent boundary layer included the correct turbulent structures at the inlet to the simulation domain. The quality of the results improved with increasing spatial resolution, as would be expected. The fact that URANS was, in this particular case, capable of capturing the mean-flow dynamics suggests that the control effects of a circular synthetic jet, in terms of time-scale, are not driven primarily by turbulence processes (small time-scale), but rather by the unsteadiness of the actuation (large time-scale). It should be noted, however, that this observation is applicable to this particular case, characterised by a low actuation frequency (=150 Hz) and a comparably small ratio between the boundary-layer thickness and orifice diameter ($\delta/d_0 = 3$). As a consequence, there was a clear spectral separation between the resolved motion (the actuation) and modelled scales (turbulence). Synthetic jets often operate within a higher frequency range with a much smaller orifice diameter, both departing from the values of the simulated experiment by an order of magnitude, and URANS is likely to become inappropriate for the simulation of practically relevant configurations, due to the violation of the spectral separation. Dandois et al. (2006) also point out that these observations only pertain to a jet in an attached turbulent boundary layer. For separated flows, for which these devices are designed, LES is expected to yield significant advantages in respect of representing the dynamics of the actuation.

Scale-resolving simulations of circular synthetic-jet injection into a boundary layer pose a number of major challenges not encountered in other flows. Perhaps the most serious one is the scale disparity between the very small jet orifice and the large body of fluid being controlled by the jet. This gives rise, on its own, to a serious grid-resolution problem. The need to resolve the near-wall region of the boundary layer, which is usually extensive in size and at high Reynolds number, substantially aggravates the resource problem. Next, the nature of the expulsion and suction phases, constituting the complete injection cycle, necessitates, in principle, the resolution of the cavity from which the jet issues and into which fluid is being drawn from the boundary layer during the ingestion cycle. This is especially important in circular-jet injection, because the jet properties at the orifice, and thus its evolution in the boundary layer, are strongly affected—considerably more so than in slot jets—by the boundary layer and by the state of the flow inside the cavity. In addition, when the working medium is air or a gas, the acoustic characteristics of the cavity are important, and Helmholtz resonance effects may be influential. However, this introduces a time-scale that is very much smaller than the injection period and also of the influential turbulent motion in the boundary layer. Yet a further problem posed by the unsteadiness is that statistically converged time-averaged and, even more so, phase-averaged data are extremely difficult to obtain, because this requires many injection cycles to be included in the simulation, and also because there are no homogeneous directions (unlike in slot-jet injection) over which integration can be performed. Finally, the boundary layer approaching the jet cannot be computed from its inception, far upstream, and this necessitates the prescription of unsteady, turbulent conditions across an inflow plane fairly close to the jet.

The present paper considers two synthetic-jet configurations: a single jet injected into stagnant surroundings and another injected into a turbulent cross-flow at zero-pressure-gradient. The aim is to gain a view of the merits and limitations of LES when applied to synthetic jets, and to provide detailed insight into the 3D physics of the interaction between the jet and the cross-flow. The results may eventually enable future research to derive simplified, reduced-order-modelling practices describing the effects of a synthetic jet in a non-scale-resolving computational environment, so as to embed synthetic-jet actuation in global simulations of industrial flows.

2. Computational framework

The simulations reported herein were performed with a general non-orthogonal-grid, block-structured, finite-volume method with a fully collocated storage, realised in the in-house code STREAM-LES (Temmerman et al., 2000) and specifically developed for LES computations. The formulation advances the velocity field in time by means of a fractional-step method incorporating a third-order Gear-like scheme documented in (Fishpool et al., 2008b) and shown to possess advantageous stability and accuracy properties, relative to a corresponding second-order scheme. The scheme may be expressed as follows:

$$\sigma_1 u_i|_{n+1} + \sigma_2 u_i|_n + \sigma_3 u_i|_{n-1} + \sigma_4 u_i|_{n-2} = -\left.\frac{\partial p}{\partial x_i}\right|_{n+1} + \sigma_5 F_i|_n + \sigma_6 F_i|_{n-1} + \sigma_7 F_i|_{n-2}, \quad (1)$$

where x_i, u_i and p are, respectively, the cartesian coordinate vector, the velocity vector and pressure, and the vector F_i contains all other terms, such as convection, diffusion and body forces. For a fixed time-step, the coefficients take the values $\sigma_1 = \frac{11}{6\Delta t}, \sigma_2 = -\frac{3}{\Delta t}, \sigma_3 = \frac{3}{2\Delta t}, \sigma_4 = -\frac{1}{3\Delta t}, \sigma_5 = 3, \sigma_6 = -3$ and $\sigma_7 = 1$. Coefficients allowing for a variable time-step are given in Fishpool et al. (2008b).

The fractional-step method advances the velocity field at time n to that at time $n+1$ in two steps. In the first step, the initial velocity field $u_i|_n$ is advanced to an intermediate field $u_i^*|_n$ by considering only the effect of the F_i term in which the fluxes are approximated with second-order central differences. Since the effect of the pressure is ignored in this step, the field $u_i^*|_n$ is not divergence-free. In the second step, an implicit calculation of the pressure field, via a pressure-surrogate of the mass-conservation equation (e.g. a pressure-Poisson equation), allows the $u_i^*|_n$ field to be *projected* onto a divergence-free field $u_i|_{n+1}$. In this second step, the pressure-Poisson equation is solved with a multi-grid method incorporating a line-implicit successive over-relaxation (LSOR) that acts as a solver and smoother. Pressure–velocity decoupling, arising from the fully collocated storage of velocity and pressure, is counteracted by employing the Rhie and Chow interpolation scheme (Rhie and Chow, 1983). Fishpool et al. (2008b) demonstrate, by reference to test computations with the above scheme for a field of 2×2 two-dimensional inviscid vortices, that the loss of energy due to artificial dissipation arising from the Rhie and Chow interpolation is very low.

The flows computed herein are treated as incompressible. The default subgrid-scale model, normally used in the code, is the dynamic model of Germano and Lilly (Germano et al., 1991). However, in the present case of jet injection into a boundary layer, there is no homogeneous direction over which averaging of the dynamic Smagorinsky constant can be effected, and some other smoothing method is needed. To this end, Lagrangian averaging, in combination with the dynamic model, as proposed by Meneveau et al. (1996), has been used.

The code is fully parallelised using MPI, with pre-determined grid blocks or sub-domains assigned to individual processors. The computations were performed, in double precision, on 64 CPUs of the high-performance computing (HPC) facility of Imperial College London. Resource requirements will be reported below in relation to specific configurations. Similarly, case-specific adaptations of the computational method, needed to accommodate particular geometric constraints, will be discussed in relevant sections to follow.

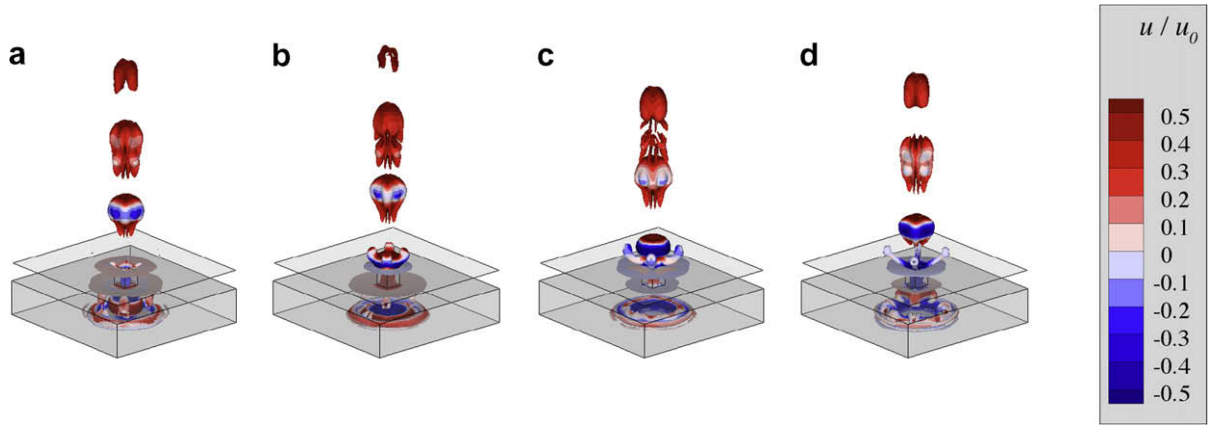

Fig. 1. Iso-surfaces of phase-averaged vorticity magnitude, overlaid with contours of streamwise velocity u/u_0, at various phases: (a) $\phi = 0$; (b) $\phi = \pi/2$; (c) $\phi = \pi$; (d) $\phi = 3/2\pi$. Obtained from a LES of a synthetic jet at $Re = 750$ issuing through a square orifice into stagnant ambient, by reference to experimental data compiled by Garcillan et al. (2004).

3. Synthetic jets injected into quiescent surroundings

3.1. Description of configuration

The practical relevance of the flow of an isolated synthetic jet in stagnant ambient conditions is relatively limited, with its usage as a cooling jet for electronic devices being a rare example of a technical application (e.g. Pavlova and Amitay, 2006). However, it is regarded as an important baseline case deserving separate study, in so far as it is a central ingredient in the control of boundary layers with synthetic jets.

In order to introduce the basic structures produced by the synthetic-jet actuation, Fig. 1 displays iso-surfaces of constant-vorticity magnitude ω obtained from a LES of a synthetic jet at a low Reynolds number of $Re = 750$, based on orifice diameter d_0 and the peak jet exit velocity, issuing through a square orifice into stagnant surroundings, by reference to experimental data compiled by Garcillan et al. (2004). A discussion of the computations and comparisons with the experimental data are provided by Wu and Leschziner (2006) and, in greater detail, by Wu (2008). In the present paper, this figure merely serves the purpose of illustrating some key features. The iso-ω–surfaces demonstrate well the evolution of the vortex ring. During the expulsion stroke, the detached shear layer rolls up to form a vortex ring above the orifice. Upon formation, the ring is then advected away from the orifice by the self-induced velocity and subsequently merges with vorticity patches that are left behind by the break-up of the ring from the preceding cycle. This process of merging triggers, in turn, the break-up of the current vortex ring prior to its diffusion in the far field.

In the present study, attention is directed towards the more challenging task of simulating the flow of a turbulent synthetic jet in a stagnant domain. This task is, arguably, more difficult than the simulation of a jet issuing into a turbulent cross-flow, the latter being the primary target of the present work. In the simulation of an isolated high-*Re* jet, the turbulent motions are entirely dependent on the jet flow itself, requiring the simulation to capture transition and represent realistically the jet-induced turbulence. The resulting turbulence statistics depend sensitively on several aspects of the simulation, among them the quality of the grid, the ability of the numerical framework to resolve the transitional process and the subgrid-scale model. Small deviations in the predicted transition location will lead to significant differences in the downstream statistics. Nevertheless, in the context of the present study, this flow shares some important characteristics with a jet injected into a boundary layer, and it facilitates the assessment of the ability of the numerical algorithm to capture the basic flow physics of the synthetic jets.

Simulations for a jet injected through circular and square orifices have been performed, by reference to experiments by Cater and Soria (2002), who conducted PIV measurements of a synthetic-jet flow in a water tank, i.e. under incompressible conditions. The flow is at a Reynolds number of $Re = 5000$ and a Strouhal number of $St = 0.003$,[1] based on the orifice diameter d_0 and the 'momentum velocity' u_0 at the nozzle, the latter being defined as:

$$u_0 = \left[\frac{1}{AT_0}\int_0^{T_0}\int_0^{A} u_{ex}(t,\underline{r})\,u_{ex}(t,\underline{r})\,dA\,dt\right]^{\frac{1}{2}}, \tag{2}$$

where A is the area of the orifice, T_0 is the period of the actuation, t is current time, r is the radial distance from the centre of the orifice and $u_{ex}(t,\underline{r})$ is the instantaneous local velocity at the orifice plane.

The computational domain includes the cavity, the orifice and the external domain. The streamwise and lateral dimensions of the external domain are $40d_0$ and $30d_0$, respectively. Both were chosen by reference to information derived from measurements. The streamwise length of the domain was chosen in accord with the regime in which near-field measurements have been conducted by Cater and Soria (2002). The choice of the lateral domain size was guided by the correlation of the half-width of the jet reported by Cater and Soria (2002):

$$r_{1/2} = S_b(x - x_s), \tag{3}$$

where S_b is the spreading rate and x_s is the axial location of the point source of the momentum jet. The experimentalists have reported a value of $S_b \approx 0.13$ for the present jet. With the length of the external domain being $40d_0$ and the point-source location, x_s/d_0, being slightly below zero, the half-width of the jet at the outlet can be estimated to be $\approx 5.5d_0$. A domain half-width of $15d_0$ thus appears reasonable in the light of the foregoing considerations.

The geometry of the cavity was treated as square-shaped, in contrast to the circular shape of its experimental counterpart. This has been done to accommodate grid-topology constraints. However, the cross-sectional area of the experimental cavity was maintained in the computations. Previous simulations of a low-*Re* synthetic jet injected into quiescent conditions (Wu and

[1] It is noted that Cater and Soria (2002) report *Re* to be 10,000, rather than 5000, and *St* to be 0.0015. However, extensive testing has revealed an error, leading the experimentalists to over-estimate *Re* and underestimate *St* by a factor 2.

Leschziner, 2006) have shown that this simplification returns a realistic jet behaviour, despite the deviations of the cavity geometry. Also, the very large experimental cavity height of $h_c = 50d_0$ was reduced to $h_c = 10d_0$, in order to lower the computational costs. This was regarded acceptable, since the flow is incompressible. As shown by Rizzetta et al. (1999), the vorticity produced at the edge of the orifice increases somewhat with decreasing cavity height, and this needs to be borne in mind in comparisons to follow. The actuation at the lower end of the cavity was imposed as a uniform sinusoidal velocity-transpiration condition, in line with the motion of the piston used in the experiment:

$$u(t) = \hat{u}\cos(2\pi ft) = \hat{u}\cos(2\pi St\frac{tu_0}{d_0}). \quad (4)$$

No-slip wall-boundary conditions were applied on solid walls inside the cavity, along the nozzle and on the plate in the external domain, while the conditions at the far-field exit of the domain were approximated by convective-outflow conditions. A constant mild influx of $0.001u_0$ was imposed as a top-hat profile on all four lateral boundaries in the external domain, so as to avoid fluid being sucked into the domain during the jet-suction phase without affecting the jet development. This option was chosen as an alternative to imposing a pressure boundary condition on the lateral boundary, a practice found to be unstable in the presence of rapid variations of entrainment and ejection associated with the suction and expulsion at the jet orifice. The magnitude of the lateral inflow velocity was chosen by reference to experimental results of Cater and Soria (2002), which show that the time-averaged and circumferentially averaged radial velocity u_r at $10d_0$ away from the centre-line is broadly constant in the axial direction, and its value was shown to be $-2\pi r u_r/(u_0 d_0) \approx 0.016$, where $r = 10d_0$. By applying mass-conservation and the square-domain circumference of $4 \times 30d_0$, the lateral velocity, to be applied on each of the four lateral boundaries, can be estimated as $u_r/u_0 \approx -0.000833u_0$. The currently employed value of $0.001u_0$ is thus a modest over-estimation of the lateral entrainment mass-flux.

Particular attention was given to the question of how to mesh the circular orifice, within the structured-grid environment of the present code. The computational code demands a rigid alignment of grid lines across block boundaries. This, and additional parallelisation constraints, preclude the use of practices involving singularities or an O-grid-topology within the orifice. Rather, the circular shape of the orifice is represented here by the meshes shown in Fig. 2, where (a) and (b) are later referred to as *deformed mesh* and *solid-cell mesh*, respectively. With the former, an originally square grid is deformed to produce a circular geometry. The deformed core mesh traverses the entire domain from the lower end of the cavity to the outflow, and hexahedral blocks are arranged around it. With the *solid-cell* approach—a variant of the Immersed-Boundary Method—an orthogonal, rectilinear mesh is used throughout the domain, and solid cells are employed to block non-fluid regions within the orifice. For comparison, a third configuration, with a square orifice having the requisite orifice cross-sectional area, is also tested (Fig. 2c), denoted by *square jet* henceforth. All three meshes contain 2.8 million cells and resolve the orifice flow down to approximately $\Delta r^+ \approx 2.5$ at the perimeter of the orifice. The expansion ratio is below 1.1 everywhere in the domain, and the cell-aspect-ratio is close to 1 in most parts of the domain. The mesh is, admittedly, somewhat coarse, and grid-dependence studies with finer meshes would be desirable. However, because of the periodic-injection conditions, computer-resource requirements are very high, even with this mesh, to achieve reasonably converged mean-flow statistics. In particular, a small time-step, of order of $\Delta tu_0/d_0 = 10^{-3}$, was required; i.e. a dimensionless period of $T_0u_0/d_0 = 1/St = 333.33$ is resolved by ca. 300,000 time-steps. As is demonstrated below (especially in Fig. 7), the mesh suffices for capturing the important features of the jet.

Time- and phase-averaged data were collected for periods given in Table 1. Computations were performed on 64 CPUs. A period of actuation was generally achieved within roughly 24 wall-clock hours.

3.2. Results and discussions

Fig. 3 shows instantaneous, phase-averaged and time-averaged flow fields of the synthetic jet injected into the stagnant environment, as returned by the simulation with the *solid-cell* technique. The first two visualisations are taken during the expulsion stroke, at the phase $\phi = 1/4\pi$, where $0 \leqslant \phi \leqslant \pi$ is the duration of the injection half-cycle and $\pi \leqslant \phi \leqslant 2\pi$ represents the suction phase. The iso-surfaces identify the locations of constant streamwise velocity $u/u_0 = 0.2$. These are overlaid with colour contours of the Q criterion, defined as $Q = 0.5(W_{ij}W_{ij} - S_{ij}S_{ij})$ (Hunt et al., 1988). A first observation arising from the instantaneous field is that the jet quickly undergoes a turbulent breakdown upon exiting the orifice. As a consequence, no distinct vortex rings can be recognised, in stark contrast to the flow structure shown in Fig. 1. The rapid transition to turbulence is associated with the high expulsion speed, and thus high Reynolds number. Consistently, both the instantaneous and phase-averaged iso-velocity contours are highly

Table 1
Run-times of various computations of the jet in stagnant ambient.

Test cast	Time-averaging	Phase-averaging
Deformed mesh	$23T_0$	$12T_0$
Solid cells	$54T_0$	$24T_0$
Square jet	$14T_0$	$14T_0$

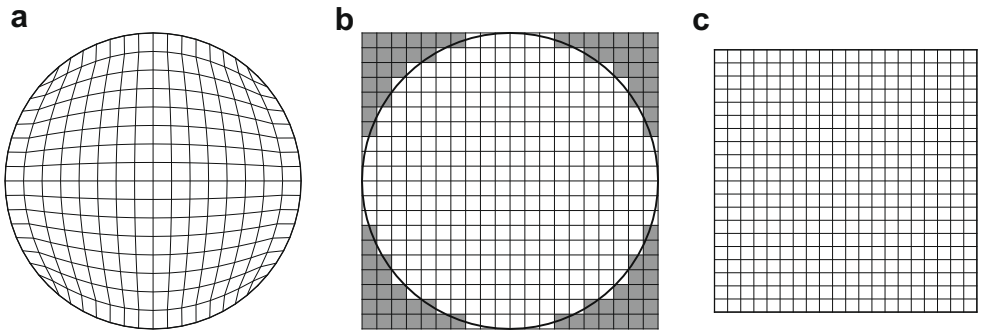

Fig. 2. Approaches to meshing the circular orifice; (a) deformed mesh; (b) solid cells; (c) square jet.

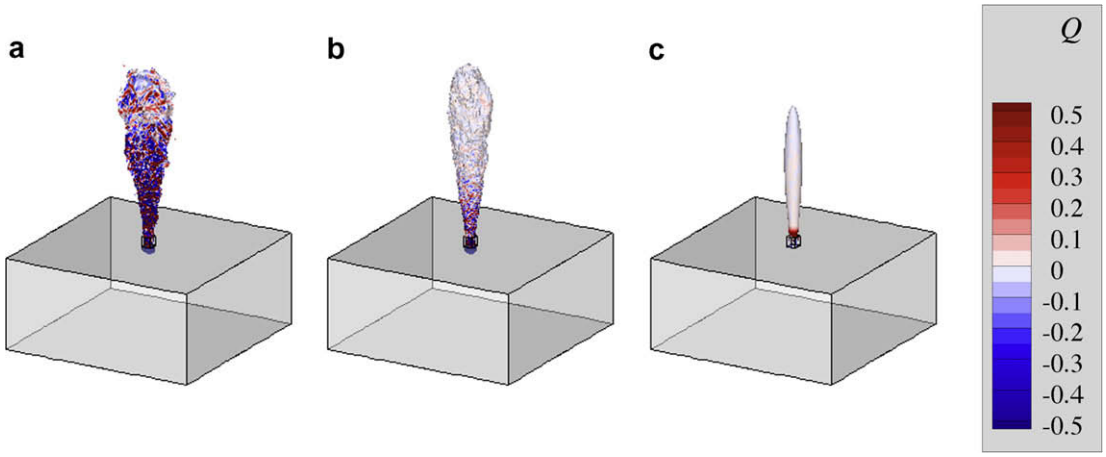

Fig. 3. Iso-surfaces of streamwise velocity u/u_0, overlaid with contours of vorticity magnitude ω, as returned by LES with the *solid-cell* approach; (a) instantaneous at $\phi = \pi/4$; (b) phase-averaged at $\phi = \pi/4$; (c) time-averaged.

elongated, the jet being well formed and continuous after only a quarter of the expulsion phase. In other words, the column (or plug) of fluid expelled is very long, covering almost the entire height of the computational domain at $\phi = \pi$. This condition is, again, very different from that shown in Fig. 1. The fact that the instantaneous and phase-averaged plots are very similar (the latter being obviously much smoother) suggests that a reasonably converged phase-averaged representation can be derived by integrating over a relatively small number of cycles. Also, the much weaker Q variations in the phase-averaged plot indicate the absence of small-scale, highly vortical features characteristic of the instantaneous field and captured preferentially by the Q criterion. As expected, the time-averaged iso-velocity surface, Fig. 3c, is smooth. The fact that this surface is considerably shorter than the phase-averaged one, the latter formed during the expulsion phase, obviously reflects the absence of upward momentum and vorticity flux over one half of each actuation period. In fact, the very existence of this elongated time-averaged iso-velocity contour provides a confirmation that, despite the mass-less injection, there results a net upward flux of momentum, similar to that in a continuous jet.

One of the aims of the present simulations is to evaluate the different approaches to representing a circular orifice in the structured-mesh environment. Fig. 4 thus shows the contours of the mean streamwise velocity in a cross-stream plane $2d_0$ away from the orifice. The most striking feature is that the *deformed mesh*, providing an accurate representation of the circular geometry, returned a near-orifice velocity that is not markedly different from that produced with the square orifice. Here, the strong deformation of the mesh (cf. Fig. 2a) comes into play, and it exerts an undesirable influence on the flow. In contrast, the fully rectilinear mesh of the *solid-cell* approach returned a much better representation of the axisymmetric flow. The *square jet* reflects, as expected, the shape of the underlying orifice, and this is obviously unrelated to the artefacts observed in Fig. 4a. Although it is reasonable to assume that the *deformed-mesh* field would become increasingly circular as the mesh is refined, the distortions in the velocity field may well diminish rather slowly, because strong mesh skewness and the near-singularities along the nominal +45 deg −45 deg diagonals are generally damaging to accuracy, however fine the grid, as a consequence of the convective flux at any finite-volume face being approximated purely by centrally averaging the nodal values lying on either side of the face in question.

Fig. 5 shows the time-averaged, normalised centre-line velocity of the jet, u_c/u_0, computed with all three orifice-shape options. Also included in the figure is an approximation for the centre-line velocity in a steady round jet, in accord with the method employed by Cater and Soria (2002), based on dimensional analysis of the far-field using the principle of conservation of momentum (Tennekes and Lumley, 1972):

$$\frac{u_0}{u_c} \approx 0.33\left(\frac{x}{d_0} + 2.3\right), \tag{5}$$

where $x_0 = -2.3d_0$ is the virtual origin of the jet. In most parts of the flow field, the agreement of the numerical results with this approximation is good in all three cases, thus suggesting that the present synthetic jet quickly adopts the behaviour of a turbulent, circular, free jet, no later than $5d_0$ away from the orifice. However, close to the outlet, Fig. 5 shows that the *deformed mesh* causes the flow to decelerate, at around $x/d_0 = 33$. This behaviour is also observed in the other two computations, albeit to a much lesser

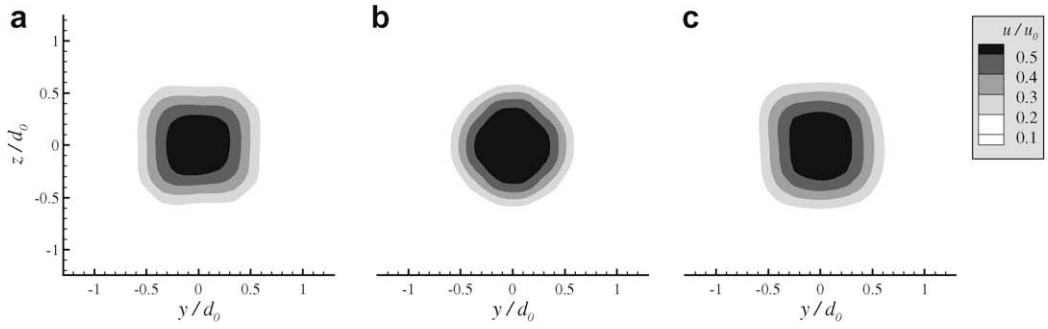

Fig. 4. Contour plots of time-averaged, streamwise velocity u_x/u_0 at the cross-flow plane $x/d_0 = 2$; (a) deformed mesh; (b) solid cell; (c) square jet.

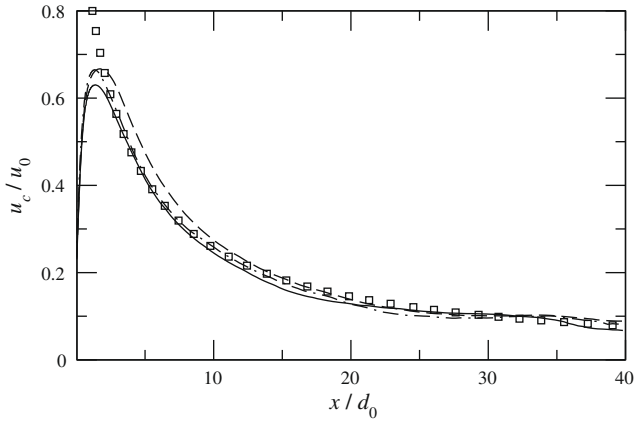

Fig. 5. Time-averaged centre-line velocity u_c/u_0; □: analytical approximation, $u_c/u_0 = [0.33(x/d_0 + 2.3)]^{-1}$; —: deformed mesh; – –: solid cells; –·–: square jet.

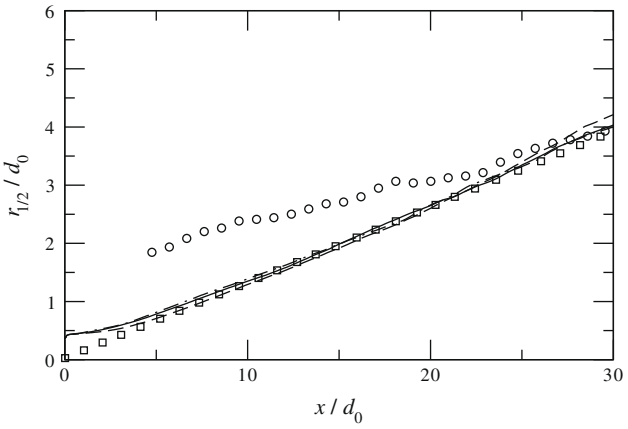

Fig. 6. Non-dimensionalised evolution of the time-averaged jet half-width $r_{1/2}/d_0$; ○: Cater and Soria (2002); □: analytical approximation, $r_{1/2}/d_0 = 1.3(x/d_0 + 0.2)$; —: deformed mesh; – –: solid cells; –·–: square jet.

extent. A reduced streamwise velocity causes a slower advection of flow structures towards the outlet, thus leading to a tendency towards a retention in the domain of fluid originating from the previous ejection cycle at the outlet. A closer examination of this behaviour has revealed that the Dirichlet velocity condition on the lateral boundaries, coupled with the chosen domain size, is not optimal for the present jet, in that it dictates the entrainment mass-flow rate, rather than allowing the solution to determine this itself. The consequence of this is that the jet is prevented from spreading freely due to the interaction with the incoming lateral flow, especially in the vicinity of the outflow. While it is possible to draw upon existing knowledge on the entrainment mass-flux in continuous jets, it has to be borne in mind that the entrainment here varies greatly in time and space, in line with the phase of the actuation. Prescribing a time-dependent inflow condition for the lateral boundaries is not a realistic proposition, however. With the Dirichlet condition being, at present, the only option in the given numerical framework, either a much larger domain has to be employed, or a more elaborate velocity prescription at the lateral boundary is required to meet the need for mass-flux associated with the entrainment. Nevertheless, this problem is not of major significance for the investigations to follow, namely the simulations for a jet in a turbulent cross-flow. In that case, the conditions at the external-domain boundaries are clearly defined by the turbulent boundary layer, and entrainment in the sense of a jet in stagnant ambient is not encountered.

With attention focused on the upstream domain $x/d_0 \leqslant 30$, Fig. 6 shows the streamwise evolution of the jet's half-width as predicted by the three computations. The agreement with the continuous-jet correlation, given by

$$\frac{r_{1/2}}{d_0} = 1.3\left(\frac{x}{d_0} + 0.2\right),$$

is good. Here, $S_b = 1.3$ is the spreading rate of the jet that was reported by Cater and Soria (2002). The fact that the experimental evolution of the half-width, reported by Cater and Soria (2002) and shown in Fig. 6, does not reflect their own spreading-rate estimate draws this particular experimental result into question. In fact, the experiments suggest an 'explosive' spread of the jet close to the orifice, and this is not borne out by any one of the simulations performed by the authors, not only for this particular configuration.

Fig. 7 shows predicted cross-stream profiles of the time-averaged velocity and Reynolds-stress components at the location of $x/d_0 = 30$, in comparison with the experimental data of Cater and Soria (2002). The radial coordinate has been normalised by reference to $\eta = r/(x - x_0)$, where x_0 is the virtual origin of the momentum jet. For all the cross-stream profiles, the agreement with the experimental data is fair to good. For both cases in which the circular orifice is represented correctly, the predicted levels of turbulence intensity and shear stress are close to the respective experimental results and to the other predicted profiles, despite the uncertainties related to the *deformed-mesh* outflow region which starts at $x/d_0 = 33$. In contrast, the results for the square jet suggest that the square orifice produces higher turbulence levels. This is plausible, since the corners of the orifice impose a higher level of strain in the expanding flow, resulting in a faster turbulent breakdown and higher levels of turbulence. As seen from the mean-velocity profiles, the streamwise velocity returned by the simulations at the edge of the jet drops below zero, indicating the presence of the reverse-flow zone close to the exit at the outer lateral region of the flow domain.

4. Synthetic jets injected into cross-flow

4.1. Description of test case

This section reports the investigation of the interaction between a round synthetic-jet and a zero-pressure-gradient boundary layer. The jet is introduced into the fully turbulent flat-plate boundary layer at an inflow momentum-thickness Reynolds number $Re_\theta = 2380$, Strouhal number $St_\infty = 0.069$, length-scale ratio $\delta/d_0 = 10$, and velocity ratio $V_R = \hat{u}_{jet}/u_\infty = 2.0$. All parameters are based on orifice diameter d_0 and free-stream velocity u_∞, in accord with the experimental configuration examined by Garcillan (2008). The domain extends from $10d_0$ upstream to $50d_0$ downstream of the injection location, while the wall-normal and lateral dimensions are $30d_0$ and $20d_0$, respectively. The jet is injected normally into the cross-flow domain, through an orifice plate with the thickness of $h_0 = 0.58d_0$. In common with the previous computations, the originally circular cavity of the experiment was approximated by a square of identical cross-sectional area. The area ratio between the cavity and the orifice is $A_R = 352$, and the cavity height is $h_c = 1.67d_0$.

The computational grid contains 7.3 million cells and resolves the boundary layer down to $\Delta y^+ \approx 0.5$, with both the streamwise and spanwise resolution being $\Delta x^+, \Delta z^+ \approx 24$ in the wake of the jet. The wall-normal cell expansion rate is below 1.1 everywhere. The maximum cell-aspect-ratio is approximately 30, being at the lateral edges of the domain in the first near-wall cell layer, due to the fine wall-normal grid, but it is below 15 in the important part of the domain where the interaction of the jet and the boundary

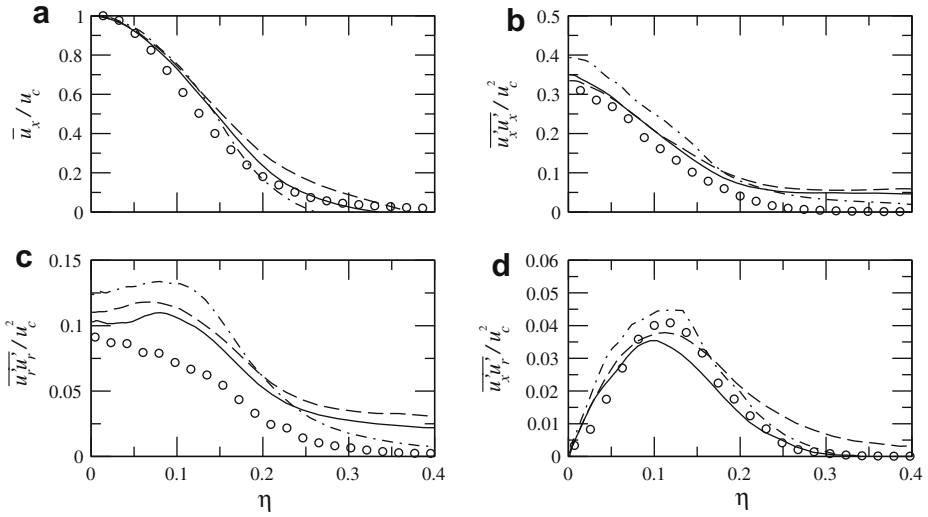

Fig. 7. Time-averaged cross-stream profiles at $x/d_0 = 30$, normalised by reference to local centre-line velocity u_c; (a) streamwise velocity $\overline{u}/u_c$; (b) streamwise turbulence intensity $\overline{u'_x u'_x}/u_c^2$; (c) radial turbulence intensity $\overline{u'_r u'_r}/u_c^2$; (d) cross correlation $\overline{u'_x u'_r}/u_c^2$; ∘: Cater and Soria (2002); —: deformed mesh; – –: solid cells; –·–: square jet.

layer takes place. These grid parameters comply with accepted guidelines for well-resolved LES for near-wall flows. The orifice is resolved by 16×16 cells. While this resolution is, again, rather coarse, it is recalled that the large disparity of the small jet orifice relative to the boundary-layer thickness (1:10) poses a considerable challenge in terms of resource requirements, especially against the background of the lack of a homogeneous direction for averaging purpose on the one hand and the need to accumulate long-time phase-averaged results on the other hand. Consequently, no grid-dependency study with finer grids has been performed. Also, the precise resolution of the structure of the jet very close to the orifice is arguably not critical to the control effectiveness in a boundary layer (as opposed to the overall momentum and vorticity influx), because the turbulence in the boundary layer exerts a dominant influence, while in the case of injection into stagnant surroundings, the structure is self-evidently more important.

The physical realism of the incoming turbulent boundary layer is secured by employing an unsteady representation of the inlet conditions, through the use of 5000 instantaneous flow realisations extracted from a separate precursor simulation for a canonical boundary layer at the required momentum-thickness Reynolds number, generated with the rescaling method proposed by Lund et al. (1998). The circular geometry of the nozzle is represented by means of the solid-cell technique, analogous to the simulation of the jet in quiescent conditions. Spanwise periodicity is imposed on the lateral ends, while the free-slip and convective-outflow conditions are employed for the free-stream and the outlet, respectively. Time- and phase-averaging were performed over a duration of 45 and 16 periods, respectively. Computations were performed on 64 parallel CPUs, with one period of actuation being computed within 7 wall-clock hours.

4.2. Results and discussions

Fig. 8 provides visualisations of the predicted phase-averaged flow fields and illustrates the structures that arise through the interaction of the jet and the boundary layer. Iso-surfaces represent areas of constant value of Q-criterion, defined earlier, while the colour/shade contours indicate the streamwise-vorticity magnitude $\omega_x(d_0/u_\infty)$. During the expulsion stroke ($0 \leqslant \phi \leqslant \pi$), as the puff penetrates deeper into the boundary layer, the lateral branches of the expelled vortex ring are stretched under the shearing influence of the boundary layer. Their sense of rotation is opposite, as indicated by the contours of ω_x, giving rise to the formation of a streamwise vortex pair. They are subsequently advected downstream by the ambient flow and soon break up into turbulent patches. Consecutive patches of iso-Q surfaces, associated to consecutive injection puffs, suggest that diffusion of the streamwise vortex pair occurs roughly $2.5T_0$ after its injection. However, in the wake of the injection, significantly enhanced level of vorticity is observed in the vicinity of the wall in the far-field, well beyond the apparent attenuation of the main streamwise vortices. Hence, this confirms the ability of the present jet to alter the external flow globally, at least $50d_0$ downstream of the orifice.

An analogous visualisation for the predicted time-averaged flow field is shown in Fig. 9. The dominant feature is a pair of streamwise vortices arising from the deflection of the jet by the boundary layer, with opposing sense of rotation as indicated by the contours of streamwise vorticity. Upon exiting the orifice, the jet is quickly realigned by the boundary layer. It is this particular structure to which the ability of synthetic jets to delay of suppress flow separation can be attributed, by increasing mixing within the boundary layer and by promoting entrainment or high-momentum fluid towards the wall.

Fig. 10 shows computed contours of the time-averaged streamwise velocity in the mid-span plane in the vicinity of the orifice. One notable feature therein is that, upstream of the orifice, the simulation indicates an acceleration in the vicinity of the wall. This is a consequence of high-speed fluid being pulled towards the wall in the upstream regime, due to the overall effect of the suction phase. A second observation derived from Fig. 10 is that the flow is deflected away from the wall as it passes across the orifice, in response to the high-momentum region established by the actuation. Downstream of the orifice, the jet formed in the blowing phase results in the formation of a small recirculation zone in the time-averaged flow-field, as indicated by the negative streamwise velocity close to the downstream edge of the orifice. It can thus be concluded that, in the time-averaged representation, the effects commonly encountered in continuous-blowing strategies arise here too, but only downstream of the injection, while upstream of the jet, the flow-field is dictated by the suction phase. As a consequence, some features normally associated with constant-blowing strategies, such as a forward stagnation point, are not encountered in the present flow.

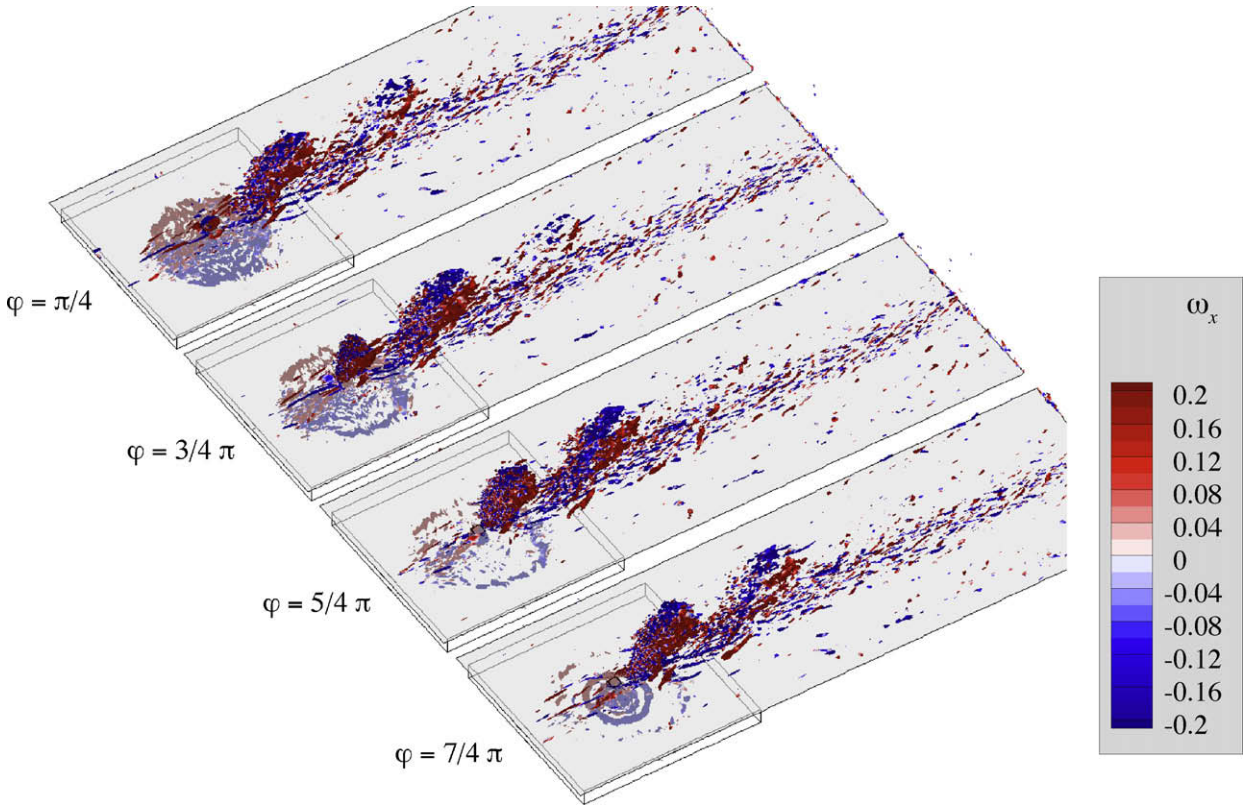

Fig. 8. Synthetic jet in turbulent cross-flow; iso-surfaces of phase-averaged Q-criterion, overlaid with contours of streamwise vorticity ω_x.

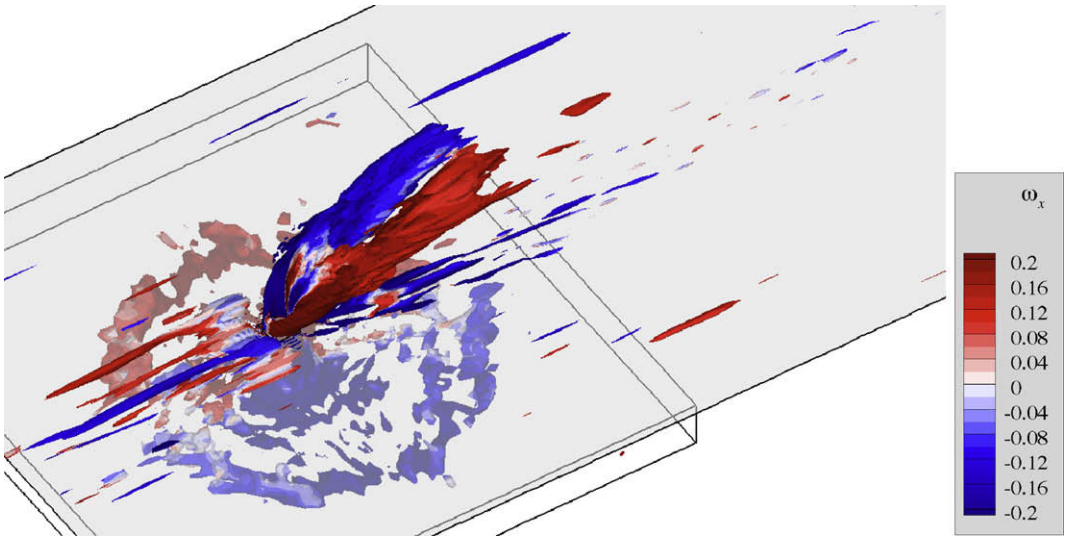

Fig. 9. Synthetic jet in turbulent cross-flow; iso-surfaces of time-averaged Q-criterion, overlaid with contours of streamwise vorticity ω_x.

A quantitative comparison of the predicted and experimental streamwise-velocity fields, close to the orifice in the mid-span plane, is given in Fig. 11. This shows four streamwise-velocity profiles at the indicated x/d_0-locations. Profiles of the baseline (no-jet) solution are also provided for comparison. The effect of the injection is to cause a wake-like depression, associated with the obstruction the jet presents to the flow. This feature is seen in the downstream profiles in Fig. 11, both in the experiment and the computation. However, at $x/d_0 = 0$, i.e. at the centre of the orifice, large qualitative differences are observed. Here, the streamwise velocity at $y = 0$ is necessarily non-zero, because the jet is deflected across the orifice, both during the injection and suction phases. The experimental data suggest that the streamwise velocity is very high in the jet, well above the free-stream velocity. This is not only counter-intuitive, but it contradicts qualitative fluid-mechanic features returned by the simulation. As demonstrated earlier, in Fig. 10, the flow above the orifice centre is deflected away from the orifice in response to the high momentum. The accuracy of the experimental resolution at this location is uncertain, possibly due to the obstruction imposed upon the orifice flow by the measurement probe.

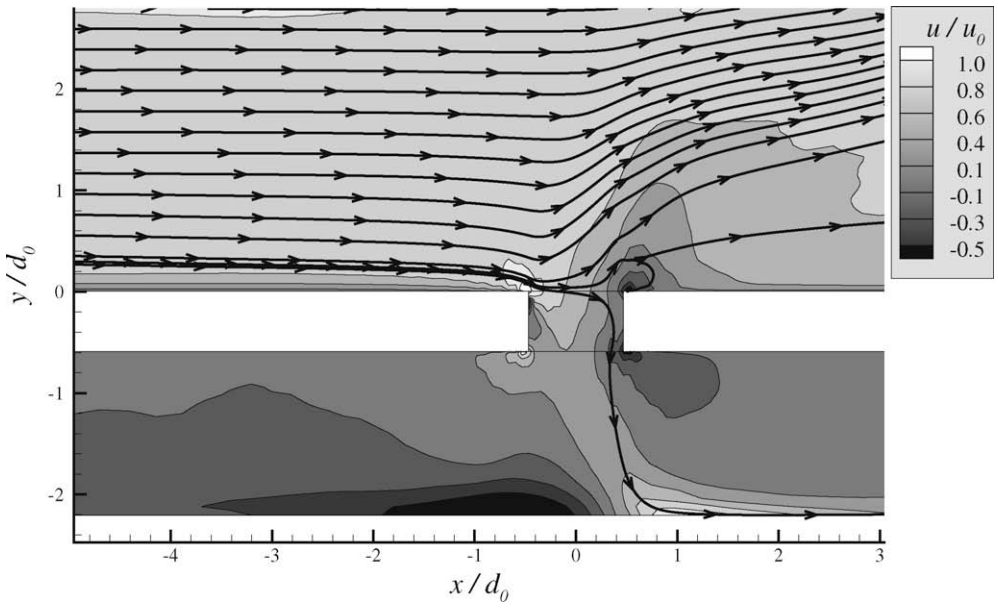

Fig. 10. Synthetic jet in turbulent cross-flow; contours of time-averaged streamwise velocity u/u_∞ in the centre plane.

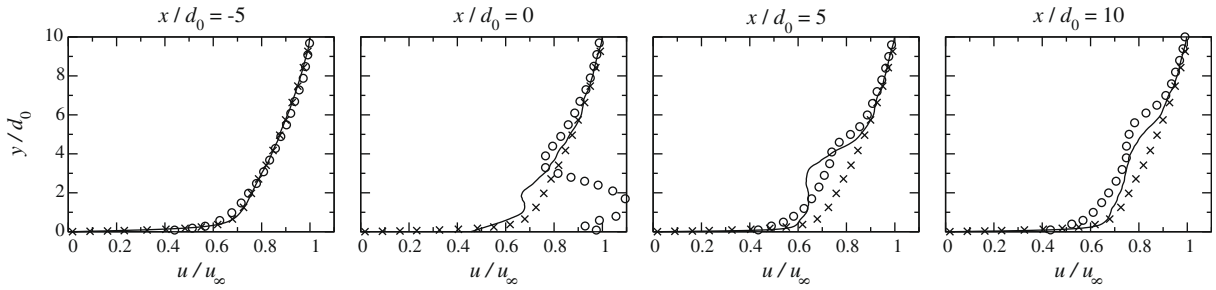

Fig. 11. Time-averaged streamwise-velocity profiles at various streamwise locations in the mid-span plane; ○: time-averaged experimental data from Garcillan, 2008; ×: LES of unactuated flow; —: LES of actuated flow.

In order to analyse the cross-flow features and spanwise effects of the actuation, contours of time-averaged streamwise velocity u/u_∞ and streamwise vorticity ω_x at four cross-flow planes are examined in Fig. 12. One striking feature is that the boundary-layer flow is asymmetric and spanwise inhomogeneous. Fishpool et al. (2008a) performed both LES and DNS of streamwise-periodic, fully developed channel flows, with two entirely independent codes, and reported substantial spanwise inhomogeneity in the long-time averaged solutions, with the observed features being long, '*streaky*' streamwise structures. The variation of the velocity magnitude in the spanwise direction was reported to be $\pm 10\%$. Fishpool et al. (2008a) show that both DNS and LES display very similar long-lived features, which are grossly argued to be physically relevant. To achieve spanwise homogeneity requires extremely long integration times, many times longer than the flush-through time.

Focusing on the effects of the injection, Fig. 12 demonstrates that, in terms of streamwise velocity (left column), the impact of the jet is limited to a spanwise distance of only $\pm 1 d_0$ on either side of the mid-span plane. At $x/d_0 = 5$, the near-wall portion of the streamwise-velocity contours, $y/d_0 < 1$, has already returned to a largely spanwise-homogeneous state, i.e. the near-wall flow in the mid-span plane has re-accelerated under the influence of the adjacent flow.

The limited spanwise influence of the actuation is underlined by Fig. 13, which shows the streamwise-velocity profiles as found in the off-centre plane of $z/d_0 = 1$, i.e. the plane that bisects the centre of one of the streamwise vortices. Except for profiles at $x/d_0 = 10$, only very minor perturbations can be seen in the cases of the actuated flows, and this confirms that the spanwise influence of the jet on the streamwise velocity is indeed limited, at least in the near-wake. At $x/d_0 = 10$, the velocity profile begins to show signs of a depression. This is related to the spanwise spreading of the streamwise vortices and the resulting widening of the 'corridor' between the vortex pair, in which low-momentum fluid is entrained away from the wall, thereby effecting a depression of the streamwise-velocity profile. The spanwise influence of the vortices thus increases as the vortices travel further downstream, prior to their diffusion in the far-field. It is noted that these observations are limited to the higher injection velocity only. At lower levels, the produced structures often fails to survive long enough, and they diffuse already before being able to reach a spanwise width that is large enough to affect the flow at this off-centre plane (Wu, 2008).

Attention is returned next to the right-hand-side plots of Fig. 12, which shows the contours of streamwise vorticity in the cross-flow planes. These bring out the pair of counter-rotating streamwise vortices produced by the injection stroke, which have a spanwise extent of approximately $2d_0$ on both sides of the orifice. Also seen is a pair of near-wall vortices formed underneath the primary streamwise-vortex pair. In order to identify the mechanism that causes the formation of these secondary vortices, contours of the phase-averaged streamwise vorticity ω_x in a wall-parallel

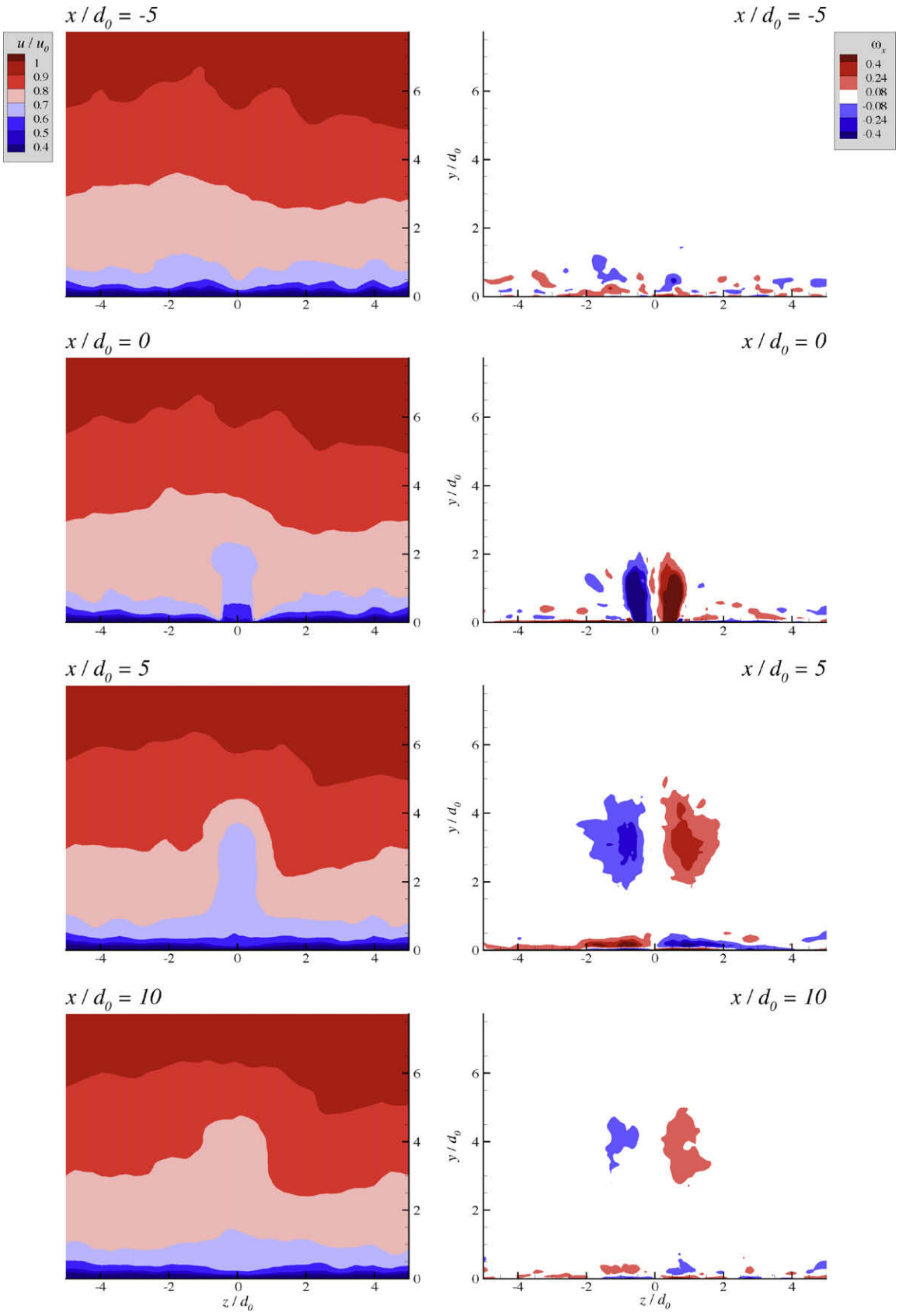

Fig. 12. Contours of time-averaged streamwise velocity u/u_∞ (left) and streamwise vorticity ω_x at four cross-flow planes.

plane at $y/d_0 = 0.15$, i.e. a plane that bisects the centre of these near-wall vortices, are examined in Fig. 14. The results are shown for the phases $\phi = 3/4\pi$ and $\phi = 7/4\pi$, supplemented by the vectors of the in-plane velocity. At $\phi = 3/4\pi$, i.e. during the blowing

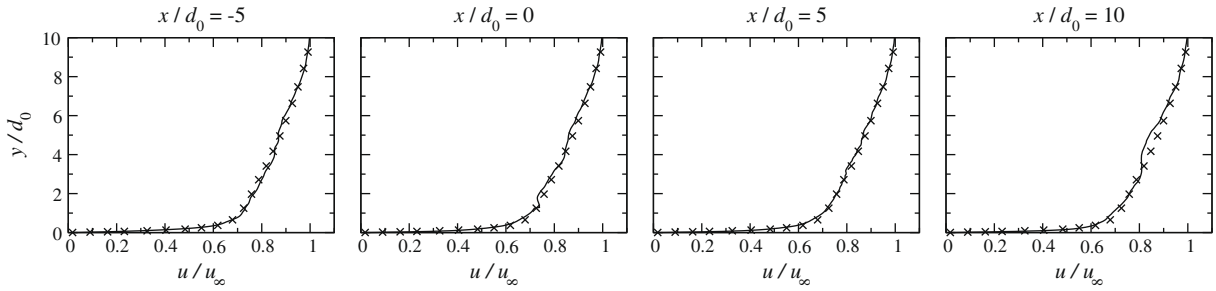

Fig. 13. Time-averaged streamwise-velocity profiles at various streamwise locations in the off-centre plane $z/d_0 = 1$; ×: LES of unactuated flow; —: LES of actuated flow.

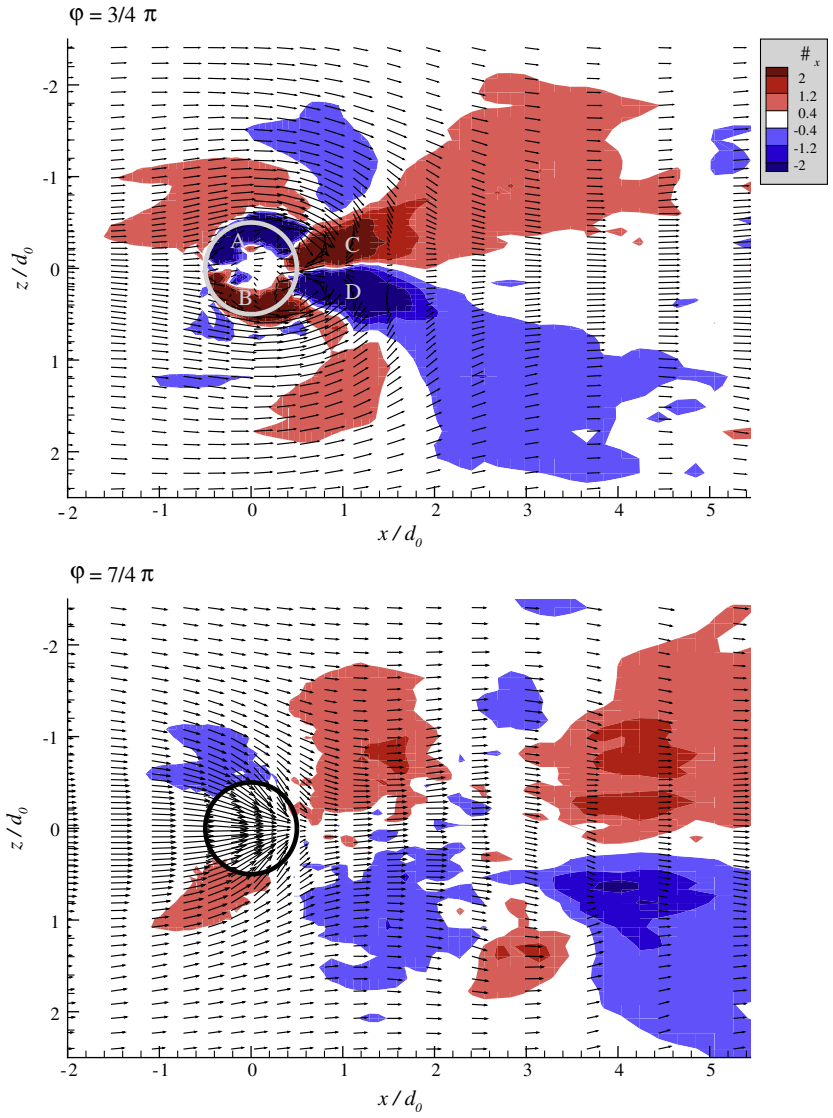

Fig. 14. Contours of phase-averaged streamwise vorticity ω_x, and velocity vectors in a wall-parallel plane at $y/d_0 = 0.15$, at two phases of the actuation cycle.

phase, two opposing streamwise-vorticity patches are seen along the lateral edge of the orifice (*A* and *B*), representing the roll-up of the vortex ring. In addition, in the wake of the orifice, the combination of the reverse flow and the inward motion of the fluid towards the low pressure wake from the lateral domain causes the pair of secondary streamwise vortices to be formed (*C* and *D*). The rotational sense of these vortices is opposite to that of the primary vortex ring at the orifice (*C* vs. *A* and *D* vs. *B*), while their vorticity magnitude is comparable. The extent of these secondary vortices, both in streamwise and spanwise directions, is relatively large. However, in contrast to the primary vortices, they lack the ability to depart from the wall and remain in the low-speed near-wall layer. As a consequence, they are exposed to a higher turbulence activity in the near-wall region, which causes a faster diffusion of these vortices, compared to the primary vortex pair. The vectors in Fig. 14 also provide some insight into the spanwise

movement of the flow in the phase-averaged sense and thereby supplements the visualisation of Fig. 10. At $\phi = 3/4\pi$, the injection is forceful and presents an obstruction to the cross-flow. Consequently, the ambient flow upstream of the orifice diverges from the centre plane. The opposite process is observed in the wake of the injection, where the low pressure region associated with the recirculation causes the lateral flow to converge towards the mid-span plane. This behaviour is entirely reversed at $\phi = 7/4\pi$. Here, the upstream flow converges towards the orifice, due to the low pressure that prevails there during the suction phase. The flow in the wake is seen to diverge slightly, presumably still biased by the previous injection stroke. The three-dimensional synthetic jet thus induces a periodic convergence and divergence of the ambient flow in the spanwise direction. This behaviour is not visible in the time-averaged flow, due to the periodicity of the spanwise motion and the removal of this effect in the time-averaging process.

Fig. 15 compares the predicted phase-averaged streamwise-velocity profiles u/u_∞ at $x/d_0 = 10$ at four different phases of the actuation. It must be pointed out first that phase-averaging encompassed only a few cycles. Also, unlike in the case of slot jets, no spanwise-averaging is possible. Hence, the computed distributions included in the figure are far from converged and should merely be regarded as providing qualitative indications. Notwithstanding these limitations, the overall agreement with the experimental data is encouraging, with the deflection of the profile at $\phi = \pi/4$ being reasonably well captured.

The global impact of the synthetic-jet actuations on the time-averaged integral quantities of the boundary layer in the mid-span position is conveyed in Fig. 16. The results are compared to corresponding values extracted by the present authors from the velocity profiles reported by Garcillan (2008). The boundary-layer thickness δ shows little sign of being affected by the injection, and this indicates that the streamwise vortices associated with the jet remain well within the boundary layer. The synthetic jet thus operates here purely as a sub-boundary-layer device. In contrast, the displacement thickness δ^* and the momentum thickness θ are significantly elevated in response to the momentum transfer imparted by the streamwise-vortex pair induced by the injection, and remain elevated for a substantial distance in terms of the injection scale d_0 (Fig. 16b and c). Both integral quantities remain well above their baseline levels, with an increase of approximately 25%. The agreement with the experimental data is reasonably good, especially when considering the uncertainties associated with processing the experimental data.

A much weaker effect of the injection on the integral quantities is observed in the off-centre plane at $z/d_0 = 1$. For that position,

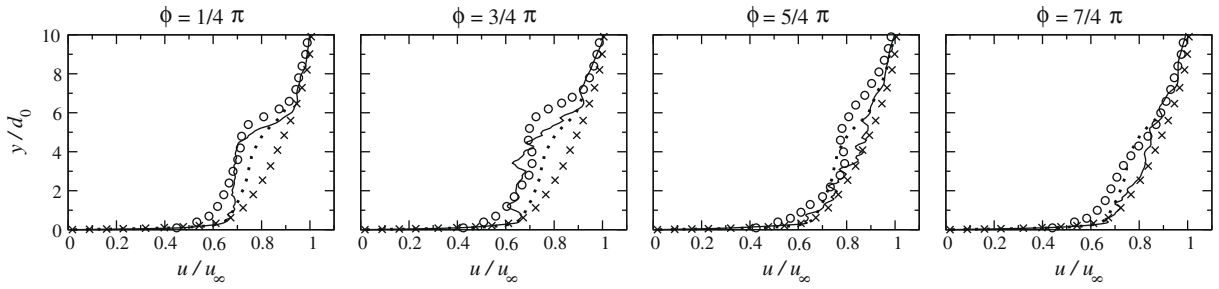

Fig. 15. Phase-averaged streamwise-velocity profiles at $x/d_0 = 10$ in the mid-span plane; ○: phase-averaged experimental data from Garcillan, 2008; ···: time-mean LES; ×: LES of unactuated mean flow; —: LES of actuated flow.

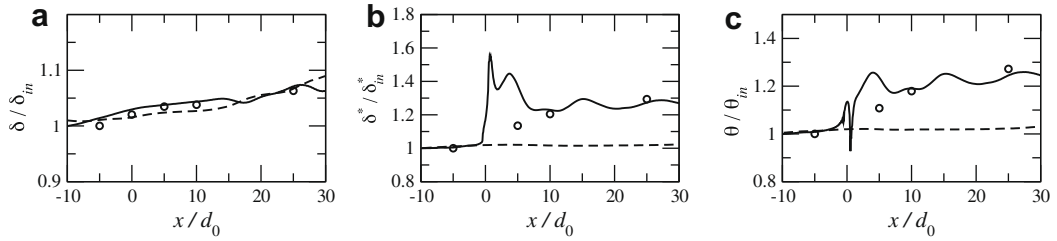

Fig. 16. Streamwise evolutions of time-averaged integral quantities in the mid-span plane; ○: Garcillan, 2008; – –: LES of baseline boundary layer; —: LES of actuated flow; (a) boundary-layer thickness; (b) displacement thickness; (c) momentum thickness.

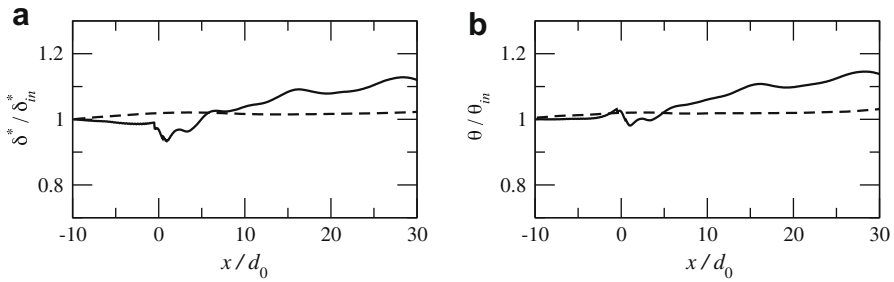

Fig. 17. Streamwise evolutions of time-averaged integral quantities; – –: LES of baseline boundary layer; —: LES of actuated flow; (a) displacement thickness; (b) momentum thickness.

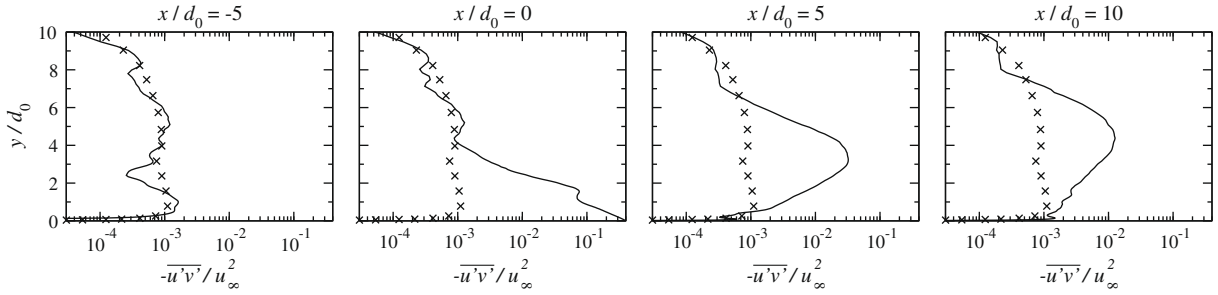

Fig. 18. Profiles of time-averaged shear stress $\overline{u'v'}$ at various streamwise locations in the mid-span plane; ×: LES of unactuated flow; —: LES of actuated flow.

Fig. 13 has previously shown that the velocity profiles in the near-wake are only weakly affected by the actuation. Accordingly, the changes of the integral quantities are initially subtle, as shown in Fig. 17. The figure suggests that δ^* and θ drop below their baseline level in the vicinity of the orifice. As the streamwise vortices widen with streamwise distance from the orifice, their spanwise influence also increases. Both integral thicknesses, δ^* and θ, regain the baseline level at $x/d_0 \approx 7.5$, and continue to grow, by up to approximately 20% in the far-field, $x/d_0 > 30$. It is noted that, for the jet at lower injection velocities, both integral quantities fail to exceed the baseline level in the far-field in this off-centre plane (Wu, 2008). This indicates that the streamwise vortices have already diffused before their spanwise extent could grow large enough to affect this lateral plane. It can therefore be concluded that a relatively forceful jet is required to perturb a reasonably wide lateral 'slab' of boundary layer. If a multiple-jet configuration is considered for flow-control applications, the ideal jet-to-jet distance will thus depend on the velocity ratio.

In the context of separation control, an important turbulence property is the shear stress, as this is the main agency for the transfer of mean momentum by turbulent motions. Fig. 18 thus displays the shear-stress profiles $\overline{u'v'}$, normalised by u_∞^2, at various streamwise locations in the mid-span plane. It is acknowledged that, for wall-bounded flows, it is common practice to normalise the turbulent quantities by the wall scales. However, here, the actuated flow does not scale with u_τ and normalisation by reference to wall scaling is not appropriate. In particular, the profile above the orifice at $x/d_0 = 0$ cannot be so normalised. Moreover, the flow downstream of the orifice is reversed. It is also important to point out that a major contribution to the shear stress in the actuated case arises from is the strong periodic motion induced by the injection, and this is one further reason for the inapplicability of wall-scaling. The upstream profile at $x/d_0 = -5$ is rather noisy due to the low number of realisations in the precursor database, coupled with the lack of spanwise-averaging.

At $x/d_0 = 0$, the injection increases the shear-stress level by over two orders of magnitude, and this can be taken to be indicative of the magnitude of the jet-induced momentum transfer across the near-wall layer. The increase of shear stress is sustained over a large portion of the boundary layer even in far distance downstream. The other shear stress components, $\overline{u'w'}$ and $\overline{v'w'}$ (not included in this paper), are increased in the immediate wake of the orifice, but they are rapidly attenuated further downstream, with negligible elevation over the baseline data beyond $x/d_0 = 5$. This again highlights the decisive contribution of the periodic fluctuations, which predominantly involve wall-normal perturbations.

5. Conclusions

The computations presented herein have demonstrated that the flow of an isolated turbulent synthetic jet injected from a cavity into a stagnant environment can be realistically captured by LES. For the particular conditions investigated, alternative meshing methods used to represent the circular orifice, either by a deformed 'H'-topology mesh, or with solid cells blocking part of a square orifice, led to only minor deviations in the time-averaged flow and turbulent-stress profiles. A square jet of the same orifice area produced higher levels of turbulence, due to the increased straining at the corners. However, the *deformed mesh* has been found to be disadvantageous to the realism of the simulation, returning a non-circular flow-field in the vicinity of the orifice, due to the strong deformation of the cells. In contrast, the flow obtained with the *solid-cell* approach returned satisfactory results. Consequently, this latter approach has been adopted for the investigation of the flow-control simulations. Despite the use of a relatively coarse computational mesh, it was demonstrated that the grid is adequate for capturing all essential features of the evolution of the jet, with the prediction of the principal properties further downstream being in good agreement with the experimental data.

For the jet-in-cross-flow configuration, the formation of a pair of streamwise vortices was shown, and these vortices were confirmed to be the major feature that is responsible for the control-effectiveness of the jet in the boundary layer. High-momentum fluid is found to be entrained towards the wall, leading to an acceleration within the near-wall layer. The displacement thickness δ^* and momentum thickness θ were both increased by roughly 25% relative to the base-line conditions. This effect is sustained beyond the observable range of the vortex pair. It confirms that synthetic-jet injection is capable of modifying the global behaviour of a turbulent boundary layer at scales that are significantly larger than the jet itself. However, these effects of the actuation are mainly limited to the mid-wake of the jet. Only when the jet spreads in the spanwise direction to a significant extent, prior to the decay of the streamwise vortices, was it possible to observe any global effects in regions well removed, laterally, from the jet-injection plane. The effectiveness of the jet thus depends strongly on the ability of the streamwise vortices to survive over a substantial distance in the wake. A relatively low injection velocity leads to a fast diffusion of the injected vortices. The shear stress $\overline{u'v'}$ is found to be elevated by up to two orders of magnitude in the wake of the injection, relative to the base-line boundary-layer flow, and this is the main agency for the momentum transfer. This very high level, surprising at first sight, is closely linked to the intense periodic motion resulting from the unsteady injection. An interesting difference to continuous-jet injection into cross-flow, at mean-flow level, is that the suction stroke leads to high-velocity fluid upstream of the orifice being entrained into the cavity, resulting in acceleration upstream of the injection and thus the avoidance, in the time-averaged field, of separation just upstream of the jet. Thus, no observable horseshoe vortex is formed around the jet.

Acknowledgement

Financial support provided for this research by the UK Engineering and Physical Sciences Research Council and BAE Systems is acknowledged. The authors are grateful to Dr. John Cater of

Queen Mary University of London and Dr. Luis Garcillan and Dr. Shan Zhong of the University of Manchester for their useful input on their respective experimental studies.

References

Cater, J.E., Soria, J., 2002. The evolution of round zero-net-mass-flux jets. J. Fluid Mech. 472, 167–200.

Dandois, J., Garnier, E., Sagaut, P., 2006. Unsteady simulation of synthetic jet in a crossflow. AIAA J. 44 (2), 225–238.

Fishpool, G., Lardeau, S., Leschziner, M.A., 2008a. Statistically persistent non-homogeneous features in periodic channel-flow simulations. In: Seventh International Symposium on Engineering Turbulence Modelling and Measurements, pp. 194–199.

Fishpool, G., Avdis, A., Leschziner, M.A., 2008b. Identification and removal of numerical instability components in low-order LES schemes. In: Seventh International Symposium on Engineering Turbulence Modelling and Measurements, pp. 22–27.

Garcillan, L., 2008. The effect of orifice orientation on the interaction of synthetic jets and turbulent boundary layers. Ph.D. Thesis.

Garcillan, L., Zhong, S., Pokusevski, Z., Wood, N.J., 2004. A PIV study of synthetic jets with different orifice shape and orientation. In: AIAA 2004-2213.

Germano, M., Piomelli, U., Moin, P., Cabot, W.H., 1991. A dynamic subgrid-scale Eddy viscosity model. Phys. Fluids A 3 (7), 1760–1765.

Greenblatt, D., Paschal, K.B., Yao, C.-S., Harris, J., 2006. A separation control CFD validation test case, part 2: zero efflux oscillatory blowing. AIAA J. 44 (12), 2831–2845.

Hunt, J.C.R., Wray, A.A., Moin, P., 1988. Eddies, stream, and convergence zones in turbulent flows. Center for Turbulence Research Rep. CTR-S88.

Krishnan, V., Squires, K.D., Forsythe, J.R., 2006. Prediction of separated flow characteristics over a hump. AIAA J. 44 (2), 252–262.

Lee, C., Hong, G., Ha, Q.P., Mallinson, S.G., 2003. A piezoelectrically actuated micro synthetic jet for active flow control. Sensors Actuators A 108, 168–174.

Lund, T.S., Wu, X., Squires, K.D., 1998. Generation of turbulent inflow data for spatially-developing boundary layer simulations. J. Comput. Phys. 140, 233–258.

Mallinson, S.G., Kwok, C.Y., Reizes, J.A., 2003. Numerical simulation of micro-fabricated zero mass-flux jet actuators. Sensors Actuators A 105, 229–236.

Meneveau, C., Lund, T.S., Cabot, W.H., 1996. A Lagrangian dynamic subgrid-scale model of turbulence. J. Fluid Mech. 319, 353–385.

Pavlova, A., Amitay, M., 2006. Electronic cooling using synthetic jet impingement. J. Heat Transfer 9, 897–907.

Rhie, C., Chow, W., 1983. Numerical study of the turbulent flow pass an airfoil with trailing edge separation. AIAA J. 21 (11), 1525–1532.

Rizzetta, D.R., Visbal, M.R., Stanek, M.J., 1999. Numerical investigation of synthetic-jet flowfields. AIAA J. 37 (8), 919–927.

Schaeffler, N.W., Jenkins, L.N., 2006. Isolated synthetic jet in crossflow: experimental protocols for a validation dataset. AIAA J. 44 (12), 2846–2856.

Smith, B.L., Glezer, A., 1998. The formation and evolution of synthetic jets. Phys. Fluids 10 (9), 2281–2297.

Temmerman, L., Leschziner, M.A, Ashworth, M., Emerson, D.R., 2000. LES applications on parallel systems. In: Parallel CFD 2000, Trontheim, Norway, May 2000.

Tennekes, H., Lumley, J.L., 1972. A First Course in Turbulence. MIT Press, Massachussets, London.

Vatsa, V.N., Turkel, E., 2006. Simulation of synthetic jets using unsteady Reynolds averaged Navier–Stokes equations. AIAA J. 44 (2), 217–224.

Wu, D.K.L., 2008. Large Eddy simulations of three-dimensional synthetic jets in quiescent surroundings and in turbulent cross-flow. Ph.D. Thesis, Imperial College, London.

Wu, D.K.L., Leschziner, M.A., 2006. Large-Eddy simulations of synthetic jets in stagnant surroundings and turbulent cross-flow. In: Morrison, J.F., Birch, D.M., Lavoie, P. (Eds.), IUTAM Symposium on Flow Control and MEMS, pp. 127–134.

Xia, H., Qin, N., 2005. Detached-Eddy simulation for synthetic jets in cross-flows using dynamic grid. In: CEAS/Ketnet Conference on Key Aerodynamic Technologies.

You, D., Wang, M., Moin, P., 2006. Large-Eddy simulation of flow over a wall-mounted hump with separation control. AIAA J. 44 (11), 2571–2577.